IEEE Access
Multidisciplinary ⋮ Rapid Review ⋮ Open Access Journal

Received 1 November 2024, accepted 20 November 2024, date of publication 27 November 2024,
date of current version 24 December 2024.

Digital Object Identifier 10.1109/ACCESS.2024.3508574

RESEARCH ARTICLE

Digital-Coding Metamaterials for On-Chip Beamsteering and Reconfigurable Millimeter-Wave Interconnects

ZHICHENG SHEN, SAJJAD TARAVATI, (Senior Member, IEEE), AND JIZE YAN
School of Electronics and Computer Science, University of Southampton, SO17 1BJ Southampton, U.K.

Corresponding author: Jize Yan (j.yan@southampton.ac.uk)

This work was supported in part by the Engineering and Physical Sciences Research Council under Grant EP/V000624/1.

ABSTRACT On-chip millimeter-wave interconnects are becoming crucial for advancing on-chip and inter-chip transmission technologies, improving transmission efficiency and system scalability, especially in Wireless Network-on-Chip (WiNoC) and chip-scale 2.5D and 3D integration. However, due to the inherent limitations of on-chip integration related to antenna size and microfabrication compatibility. On-chip wireless channels often necessitate the use of compact, planar antennas. These antennas typically suffer from limited transmission gain, lack of beam control, and poor interference immunity, posing challenges to the reliability and versatility of millimeter-wave interconnects. This paper presents a 1-bit digital-coding metamaterial to address these challenges. The metamaterial features a 3×5 tunable unit-cell array, with each cell switchable between the '0' or '1' state with a distinct refractive index. The refractive index distribution within the unit cell array can be controlled through different binary coding sequences to manipulate the electromagnetic waves and achieve different transmission functions. When integrated with an on-chip dipole antenna, the metamaterial can achieve adjustable beamsteering in the range of $\pm$ 40°, 3.3 dB transmission gain enhancement, 90° beam splitting, and efficient energy attenuation. The proposed digital-coding metamaterial allows precise control and reconfiguration of the wireless signal distribution on silicon, significantly enhancing the flexibility, efficiency, and scalability of on-chip millimeter-wave communications.

INDEX TERMS Electromagnetic metamaterial, beamsteering, millimetre-wave, intra-chip interconnects, wireless network-on-chip, interference, digital-coding metamateiral, antennas and propagation.

I. INTRODUCTION

The rapid advancements in semiconductor technology have paved the way for increasing the integration and miniaturisation of electronic components. Conventional wired interconnects face significant challenges, including increased power consumption, latency, and area overhead due to parasitic capacitance and inductance. Integrated wireless interconnects offer a promising solution to these issues by using micro-antennas and transceiver modules to transmit and receive signals via electromagnetic (EM) wave propagation within the silicon chip. Their advantages have been demonstrated in multiple fields of application. In Wireless Networks-on-Chips, the wireless data transfer between two distant nodes can significantly reduce hop counts and overall transfer delay compared with a pure wired architecture [2], [3], [4]. In wireless clock distribution networks, the average clock delay, power consumption and maximum clock skew are noticeably reduced compared with conventional H-tree clocks [18], [19]. In heterogeneous 2.5D and 3D integration, wireless interconnects help to reduce the wiring complexity and integration cost [13], [27].

On-chip antennas are typically designed and fabricated on the top metal layer of modern CMOS processes or within the metal interconnect layer of silicon interposers [7], [12], [18]. Due to these integration constraints, most on-chip millimeter-wave antennas are implemented as planar patches [11], [23], [26], monopoles [1], [6], [13], inverted-F

The associate editor coordinating the review of this manuscript and approving it for publication was Tutku Karacolak.

[10] and dipole structures [14], [15], [16], which exhibit omnidirectional or low-directivity radiation patterns. On-chip millimetre-wave interconnects based on low-directivity antennas typically carry broadcasting transmission mode. Figure 1(a) presents the schematic design of a broadcasting intra-chip interconnect that features broad transmission coverage; each transmitter antenna can effectively cover a large chip area with minimal signal dead zones. Broadcasting interconnects are particularly suitable for applications such as wireless clock distribution networks [18], [19]. However, the simultaneous activation of multiple transmitters can lead to significant signal interference due to overlapping radiation regions. Broadcast interconnects often employ a token-passing-based medium access mechanism to avoid interference [3], [5], but this approach increases transmission delay and reduces the efficiency of wireless medium utilisation.

High-directional antennas offer an effective solution to reduce interference caused by overlapping radiation regions. H. K. Mondal et al. proposed a directional on-chip log-periodic antenna coupled with an interference-aware placement algorithm, demonstrating low-interference millimeter-wave links within a 64-core Network-on-Chip (NoC) system [8], [9]. Similarly, V. Pano et al. showcased a WiNoC design using bi-directional antennas, achieving a 66% reduction in channel interference through an innovative substrate propagation technique [17]. Figure 1(b) depicts the schematic of a high-directional intra-chip interconnect. The directional antennas allow the construction of multiple non-interfering interconnects on the same silicon, facilitating parallel transmission and improving overall data throughput. In addition, high directivity enhances transmission gain and improves energy efficiency. However, the constraints of on-chip integration prevent the implementation of any mechanical beam scanning mechanisms. The radiation direction of each antenna is fixed and can only cover a small area of the chip, greatly limiting the flexibility of transmission. Additionally, antenna sidelobes may still cause interference with neighbouring antennas, potentially degrading the transmission quality.

This paper proposes an on-chip digital-coding metamaterial for intra-chip millimeter-wave interconnects, which empowers the on-chip antenna with diverse beamsteering capability to adopt a variety of transmission needs. Metamaterials are artificially engineered structures designed to manipulate electromagnetic waves under a certain range of frequencies. They feature periodic structures formed by sub-wavelength meta-atoms (Unit cells), which are designed to obtain irregular electromagnetic responses. The beam-steering metamaterial has significantly evolved over the past two decades, particularly in 5G-related applications [41], [46]. Early research focused on gradient-index (GRIN) metamaterials and reconfigurable metamaterials, which deflect beams by creating spatially varying refractive indices across the material. Typical GRIN can achieve a beam deflection angle from 15° to 60° depending on the antenna type and the metamaterial footprint [30], [32], [35]. The reconfigurable metamaterials contain unit cells that can be electrically or optically switched between two refractive indexes, thus switching the beamsteering angle between positive and negative values [31], [33], [34]. However, reconfigurable metamaterials have difficulty in achieving fine-tuning of the antenna beam direction due to the limited reconfigurable state of the metamaterial.

Digital-coding metamaterials and metasurfaces represent a significant advance in beam-steering capability. These metamaterials consist of tunable unit cells with discrete states that can be represented by 1-bit or multi-bit binary coding, allowing for various beam control functions through different coding combinations. The digital-coding sequence greatly enhanced the control freedoms of metamateiral, which enables dynamic and precise control of beam deflection angles. Cui et al. pioneered the design of a 1-bit coding metasurface embedded with PIN diodes, capable of creating different scattering patterns through digital coding sequences [36], [37]. Existing digital-coding metamaterials can achieve a beamsteering accuracy of 10° to 15° over a range of ±45° [37], [38], [39]. The 2-bit and multi-bit coding metasurfaces and multi-bit coding allow finer control over the phase state distribution across the metamaterial [36], [40]. Under the real-time control from a digital programming unit (typically a FPGA or ASIC), the digital-coding metamaterial can perform advanced beam-steering and beamforming functions, such as multi-dimensional, [36], [47], time-modulated [51], [53] and nonreciprocal [39], [51], [52] beamsteering, RCS reduction [44], orbit angular momentum (OAM) generation [45] and holography display [44].

Digital-coding metamaterials offer significant advantages in beam-steering accuracy, versatility, and flexibility compared with other approaches. In this work, the main idea is to combine the coding metamaterials with on-chip millimetre-wave transmission. The powerful digitally coded metamaterials can effectively compensate for the lack of beam control capability of on-chip antennas. The planar metallic structure of the metamaterial makes it suitable for on-chip integration. For WiNoC and other related intra-chip millimeter-wave interconnects with constantly changing requirements on the transmission targets and direction, digital-coding metamaterials can effectively meet the relevant needs with their high-precision and diverse beam deflection capabilities.

The remaining sections of this paper are organised as follows: Section II presents the design of a 1-bit coding unit cell through topological optimisation. Section III presents the design of the digital-coded metamaterial for on-chip beam-steering. Section IV presents the RF transceiver circuit design and intra-chip simulation setup for beam-steering and reconfigurable transmission analysis. Section V provides the simulation results, showing ten different transmission modes achieved by the proposed digital-coding metamaterial under

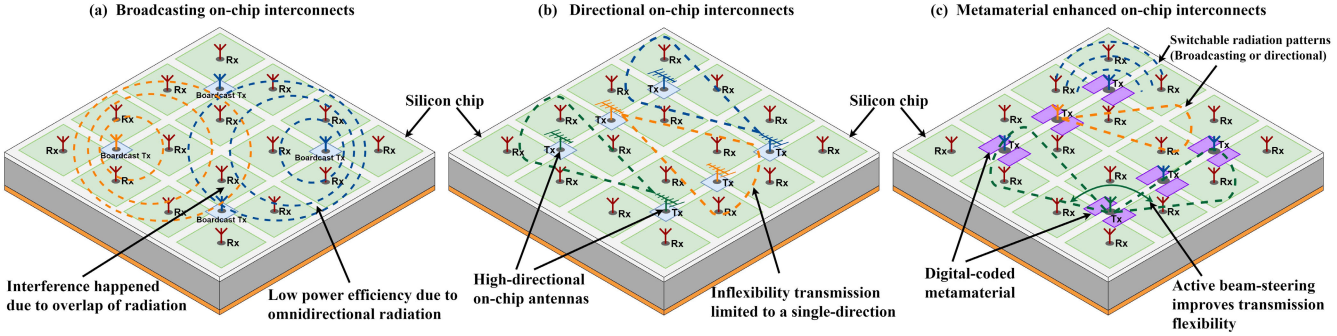

FIGURE 1. Schematic diagram of on-chip millimetre-wave interconnect based on different antenna types. (a) Omnidirectional broadcasting antennas. (b) Directional antennas and (c) Proposed metamaterial enhanced antennas. The digital coding metamaterials (Purple regions) feature each transmitter antenna with large-angle beam steering and multiple transmission modes, and each metamateiral can be reconfigured to generate the most appropriate radiating pattern dependent on the transmission target.

different coding sequences, and compares its performance with other on-chip beam-steering approaches. Section VI provides an overall summary of the paper.

II. CONCEPT AND DESIGN

A. METAMATERIAL-ENHANCED ON-CHIP INTERCONNECT

Section I reviews two conventional on-chip wireless interconnect designs: one based on broadcasting antennas (Fig. 1(a)) and the other on directional antennas (Fig. 1(b)). Due to the lack of on-chip beamsteering methods, on-chip millimeter-wave interconnects suffered from challenges like low interference immunity and poor transmission flexibility. In this work, we introduce integrated digital-coding metamaterials into the on-chip wireless interconnects, which can actively manipulate the radiation pattern to create different transmission modes.

Figure 1(c) presents the schematic design of metamaterial-enhanced on-chip millimeter-wave interconnects. The purple area indicates the on-chip metamaterials placed closely with each transmitter antenna for active radiation control. The introduction of metamaterial could remarkably improve the transmission flexibility of millimeter-wave interconnects. Each transmitter antenna antenna can support a large-angle beam-steering, and multiple adjustable radiation patterns include both high directivity and broadcast transmission. The metamaterial can function as an EM absorber under a specific configuration to reduce interference caused by antenna sidelobes or unwanted radiation. Parallel transmission with multiple on-chip wireless interconnects can be achieved by properly configuring multiple sets of metamaterials to avoid overlap of radiation. The transmission direction and coverage area of each antenna can be reconfigured and optimised based on transmission objectives. Overall, metamaterial-enhanced on-chip interconnects combine the advantages of both broadcast and high-direction interconnects, offering broad transmission coverage and high-gain parallel transmission. Their primary issues are effectively mitigated, which are poor interference control and fixed transmission direction.

B. DESIGN OF THE TOPOLOGY UNIT CELL

The basic design unit of a metamaterial is the unit cell, a specially designed metal patch that interacts with incoming EM waves to achieve certain dielectric properties. This paper introduces a novel circular-shaped unit cell design based on topology optimisation. Figure 2(a) presents the design procedures of the unit cell from a circular sector metal patch. The circular sector patch has a radius of R and a central angle δ. The path is then divided into P lines and Q colours of annulus sectors with a smaller central angle δ/P, and a small circular sector near the centre with a centre angle of δ and radius of $R/(Q+1)$. Each small sector can be present in either a bit 1 or bit 0; bit 0 indicates an absence of metal within the pixel area, while bit 1 represents the pixel existence of metal in that area. In our unit cell present in Fig. 2(a), where $P = 4$, $Q = 9$ and $\delta = \pi/2$ rad. The optimisation region contains 36 annulus sectors and one circular sector, which requires 37 bits to define a pattern. Following the pixel mapping, the defined ring sector is rotated by 90° for 4 times to form a complete circular unit cell design.

The arrangement of the pixel map on the unit cell creates capacitive and inductive structures. Different pixel maps will change the total equivalent capacitance C_t and inductance L_t until resonance frequency matches with the optimal target. The resonance frequency of the unit cell can be approximated as [41] and [42]:

$$f_r = \frac{1}{2\pi\sqrt{L_t C_t}}. \tag{1}$$

The size of the unit cell is approximately 1/9 of the target optimisation wavelength λ_0. The unit cell is simulated on a multi-layer silicon substrate present in Fig. 2(b). It comprises several metal and insulator layers from the bottom to top: a 1 μm metallic ground layer at the bottom, a 625 μm thick silicon substrate and a 2 μm thick SiO_2 insulating layer separating the antenna and metamaterial layer from the silicon substrate. The field setup simulates the TE mode millimetre-wave propagation inside the dielectric silicon

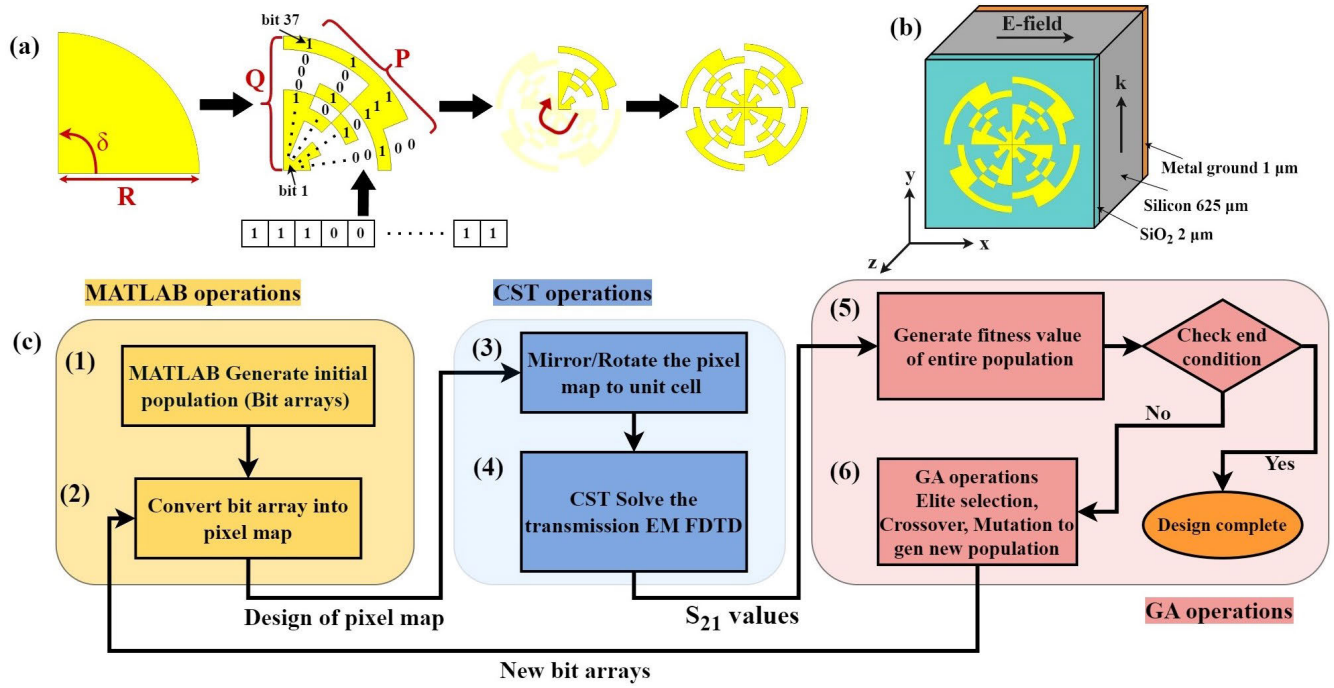

FIGURE 2. Pattern generation, coding and optimisation process of the topological metamaterial unit cell. (a) Design process of the unit cell. A circular sector metal patch is coded with a 37-bit binary sequence in either '1' or '0', then rotated four times to form a complete cell. (b) The simulation setup of the unit cell on a multi-layer silicon substrate. (c). The flow chart shows the optimisation process based on the genetic algorithm performed through MATLAB and CST simulation.

substrate generated by an on-chip dipole antenna [43]. The EM wave is propagating at the *y*-axis, and the electric field is perpendicular to the direction of propagation on the *x*-axis.

C. OPTIMIZATION FLOW

The topology optimisation process of the proposed metamaterial unit cell is performed using a MATLAB-CST co-simulation in Fig. 2(c). The optimisation combines the full-wave simulation in CST and a pattern generation and selection script based on genetic algorithm (GA) in MATLAB. A similar flow has shown its effectiveness in optimising multiple metamaterial parameters in previous publications [54], [55], [56]. The optimisation begins with an initial population that can be randomly generated by MATLAB or pre-defined by the user. This population comprises multiple individuals, each representing a 37-bit binary sequence used for coding the circular sector. The binary sequences are then mapped to the pixels to generate the sector design. The map design is transferred to CST through the CST-MATLAB Interface. CST rotates and duplicates the pixel map to create a complete unit cell pattern and simulates the unit cell under the condition given in Fig. 2(b). This process is repeated until all individuals in the first population are analysed.

After the simulation, the S-parameters results are passed back to MATLAB for GA operations. Firstly, the fitness value of the entire population is calculated based on a user-defined fitness function. Then, an end condition check determines whether any individual has reached the fitness limit. If the limit is reached, the program records the binary coding of the best fitness design and terminates. If not, the population are sent to GA operations, including elite selection, crossover, and mutations, which generate the next population of binary sequences. This new population is used to code new pixel maps, and the optimisation cycles are repeated until a fitness limit is satisfied or the maximum population count is reached.

During the GA operations, the population size is set to 10-15. The crossover probability is set as 0.8. The number of elite children per generation is 1. The mutation rate is 0.01. The end condition consists of a fitness limit value and a maximum generation limit of 30 to prevent the program runs forever. It is worth noticing that a small population of 10-15 is used compared with the coding length (37) of the pixel map. It helps to shorten the simulation cycle and fasten the convergence of the genetic algorithm. However, this may cause its tendency to converge towards the local optima position. To overcome this problem, multiple GA optimisation processes are repeated using different initial populations to quickly search for multiple locally optimal designs. After that, the locally optimal designs are selected and compared to generate one to two final optimised designs.

The fitness value defines the target of optimisation on the metamaterial unit cell. In this paper, we focus on the optimisation of two targets at the same time: the resonance frequency of the unit cell and the incident angle sensitivity of the unit cell. The resonance frequency defines the operation

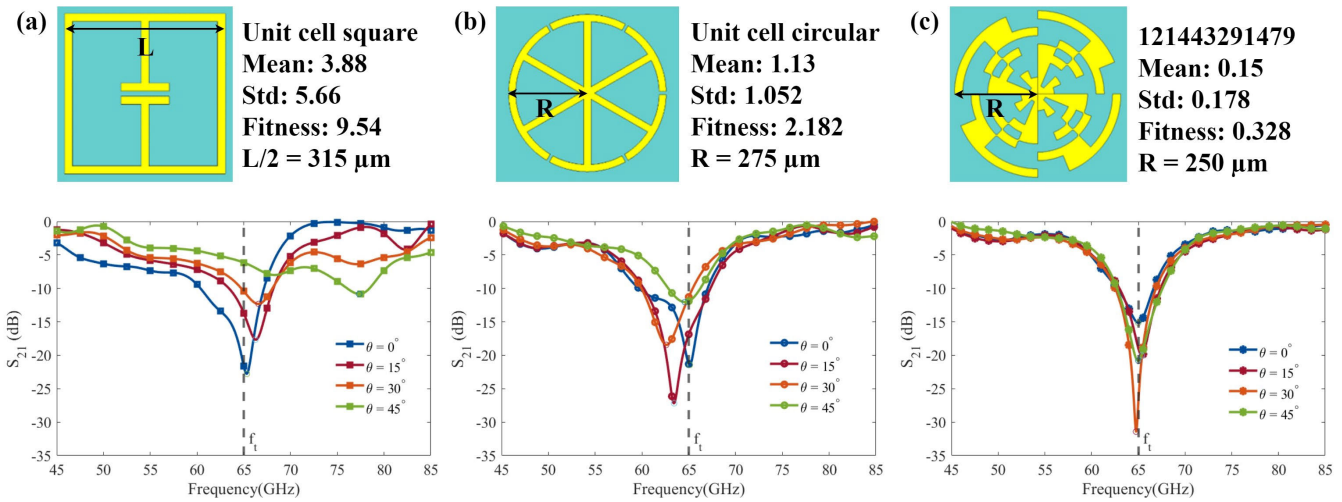

FIGURE 3. Comparison of the optimised unit cell with two conventional unit cell designs under different signal incident angles from 0° to 45°, each figure presents the mean and standard derivation of resonance peak shift, fitness value and the S_{21} curve under the four angles. The layout of (a) a conventional squared unit cell shows poor resonance consistency when the incident angles increase, and (b) a circular unit cell formed by three 'barbell' shaped resonators with better angle independence. (c) The topologically optimised unit cell has the highest resonance consistency with one order of magnitude reduction in the fitness value.

band of the metamaterial, which should be as close to the target frequency f_t. The incident angle sensitivity defines the resonance consistency of the metamaterial under different signal incident angles of 0°, 15°, 30° and 45° (Achieved by rotated the unit cell by the corresponded angle around its centre point), which should be as consist as possible. The fitness function can be expressed as:

$$fitness = \min(a \cdot \text{std}(|f_p - f_t|) + b \cdot \text{mean}(|f_p - f_t|)), \quad (2)$$

where f_p is the resonance peak frequency of the unit cell, and $|f_p - f_t|$ is the absolute difference between the peak frequency and the target frequency. This fitness function target minimises the mean and standard deviation (std) value of the frequency difference under four incident angles. The a and b are weights parameters, which were both set to 1 in this case.

D. OPTIMIZATION RESULTS

Figure 3(c) presents the layout of an optimised unit cell with serial number 121443291479, corresponding to the decimal format of the 37-bit binary sequence defining its pattern. Two conventional unit cell designs are also shown in Fig. 3(a) and Fig. 3(b) for comparison. The labels on the right of each cell layout provide the mean and standard deviation of the resonance peak shift under four angles, as well as the fitness value of optimisation and the radius of the unit cell. The figure below plots the S_{21} curve pf each cell under signal incident angles of 0°, 15°, 30°, and 45°. The black dotted line indicates the target optimisation frequency f_t at 65 GHz.

The square-shaped resonator in Fig. 3(a) exhibits resonance performance highly dependent on the incident angle due to its nonsymmetric diagonal and vertical directions. The resonance peak shifts towards higher frequencies and quickly attenuates as the incident angle increases, resulting in high mean and standard deviation values. Figure 3(b) presents a circular-shaped unit cell design that is formed by three barbell-shaped resonator structures that are rotated and duplicated around its centre point. This design approach gives the unit a symmetrical nature under multiple angles, which lowers the fitness value by a factor of 4.37 compared to the squared cell. However, the S_{21} curves show that there is still a maximum peak offset of around 2.4 GHz under 15° and 30° incidence angles.

The topologically optimised unit cell takes this improvement further, achieving an average frequency shift of 0.15 GHz and a standard deviation of 0.178, with nearly an order of improvements in fitness value compared to conventional designs. The S_{21} plots indicate almost no shift in the peak resonance frequency from 0° to 45°. Additionally, the radius of the optimised unit cell is 9% smaller than the conventional circular unit cell, saving 17% of area per unit cell. We achieve a compact and angle-independent metamaterial unit cell design through topology design optimisation. The unit cell can guarantee highly consistent performance at different beam deflection angles, which lays the foundation for equivalent refractive index calculations and the following metamaterial design. Moreover, its pixelated structure also benefits the tunable design required by digital-coding metamaterial; the resonance modes of the unit cell can be significantly changed between two or multiple states by identifying and changing one or more critical pixels.

E. DESIGN OF ONE-BIT CODING UNIT-CELL

The design of the one-bit coding unit cell is derived from the optimised cell '121443291479' with a radius of 250 μm. The pixel 31 in the unit cell is identified as the critical pixel,

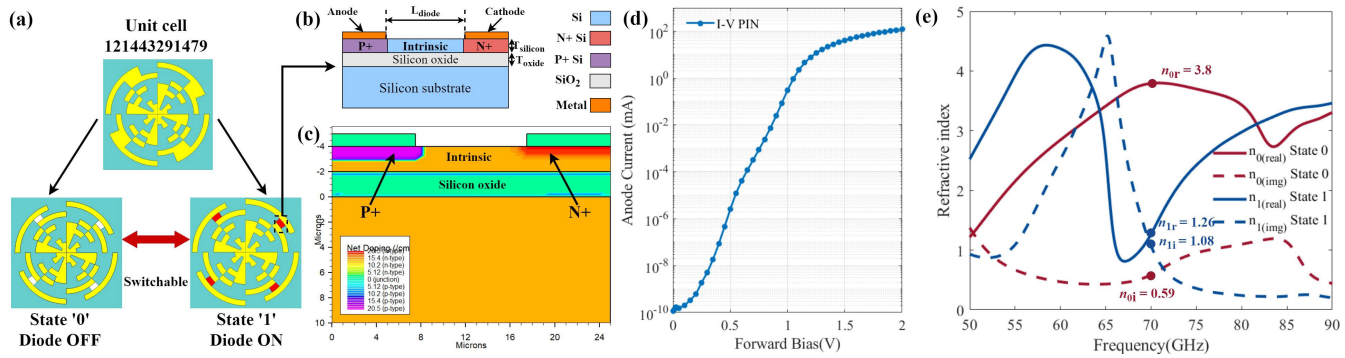

FIGURE 4. Design and characteristics of a 1-bit coding unit cell. (a) The coding unit cell modified from optimised cell '121443291479', a tunable PIN diode replaces the metal on pixel 31 to achieve two switchable states: '0' when the diode is switched OFF and '1' when the diode is ON. (b) The cross-section view of the tunable on-chip PIN diode, heavily doped P+ and N+ areas are formed below the anode and cathode, and a lightly doped intrinsic region is in the middle. The anode and cathode are directly attached to the metallic pattern of the unit cell. (c) The net doping diagram of the PIN junction was simulated with the Silvaco TCAD. (d) I-V characteristic of the PIN diode with a forward bias voltage from 0 to 2 V. (e) Real and imaginary parts of the effective refractive index *n* when unit cell under state '0' and '1'.

which is replaced by a simple electrically controlled diode. The unit cell has two operating states that depend on the diode configuration on the critical pixel 31, which can be expressed by a 1-bit binary code in either '0' or '1'. The state '0' presents all diodes as switched OFF, and pixel 31 is insulating. State '1' is defined when all diodes are switched ON, and pixel 31 is conductive.

The PIN diode has been widely used as the switching component in previous reconfigurable and digital coding metamaterials [33], [37]. In our case, a planar SOI PIN diode is chosen as the tunable pixel, as its simple structure can be easily integrated with the planar metallic pattern of the on-chip metamaterial, and it is fully compatible with standard CMOS fabrication processes [57], [58]. The cross-section structure of the PIN diode is present in Fig. 4(b). The diode is fabricated on a typical SOI substrate, and the P-I-N structure is formed on the top device layer of silicon. Figure 4(c) presents the doping map of the diode simulated with Silvaco TCAD; the P+ and N+ regions are doped with ion implantation with a concentration of 1×10^{19} atoms/cm^3 and followed by a short anneal. The intrinsic region is lightly doped with phosphorus with a concentration of 1×10^{14} atoms/cm^3. The anode and cathode are metal patches extended from the metallic structures of the unit cell. The length of the intrinsic region L_{diode} is 10 μm, and the thickness of SiO_2 and poly-silicon layer T_{silicon} and T_{oxide} are both 2 μm. The I-V response of the PIN diode is presented in Fig. 4(d). When no or little forward bias is applied to the diode, the PIN diode works as a large resistor due to the presence of the intrinsic layer between the anode and cathode. When the forward-biased voltage reaches 2 V, the diode is fully switched on, and the free carriers are injected into the intrinsic region, which remarkably reduces the resistance of the diode to around 5 Ω.

The one-bit coding unit cell exhibits two different frequency responses under the state '1' and state '0'. Figure 4(e) plots the simulated effective refractive index n versus the frequency under the two states. At 70 GHz, the state '0' unit cell has a high real part of $n_{0\text{r}} \approx 3.8$ and a low value on the imaginary part $n_{0\text{i}} \approx 0.59$. State '1' performed oppositely, with a much lower real part $n_{1\text{r}} \approx 1.26$ and a higher imaginary part $n_{1\text{i}} \approx 1.08$ compared with the state '0'. The real part and imaginary part affect the phase velocity and the loss of the signal passing through the metamaterial. The state '0' unit cell has a high deflection capability and low signal loss, whereas state '1' has a much lower deflection capability but much higher signal loss. The index difference between the two states forms the basis for beam-steering applications.

III. DESIGN OF DIGITAL-CODING METAMATERIAL

Figure 5(a) sketches the proposed digital-coding metamaterial design based on the two-state tunable unit cell. The metamaterial consists of a 3 × 5 array of unit cells on the same multi-layer silicon substrate in Fig. 2(b). The adjacent unit cells have a horizontal and vertical separation of 100 μm. The configuration of the metamaterial can be represented by a 15-bit binary coding, and each bit corresponds to the switching state of the unit cell at the given position. Due to the difference in the equivalent refractive index under states '0' and '1', the unit cell array can form an inhomogeneous refractive index distribution after coding, which causes deflection when the electromagnetic waves pass through the metamaterial, and different coding sequences will lead to different deflection angles.

An on-chip meandering dipole antenna (MDA) is placed below the metamateiral to serve as an electromagnetic source. It comprises two metal strips placed end-to-end, each with 11 repeated meander sections. The meander section is characterised by the parameters arm length (l), arm width (w), line width (b) and thickness (t). The MDA in this paper operates at 70 GHz, with $l = 18$ μm, $w = 12$ μm, $b = 5$ μm, $t = 1$ μm. The metal strips are connected to GSG contact pads for port signal feeding. Each pad has a size

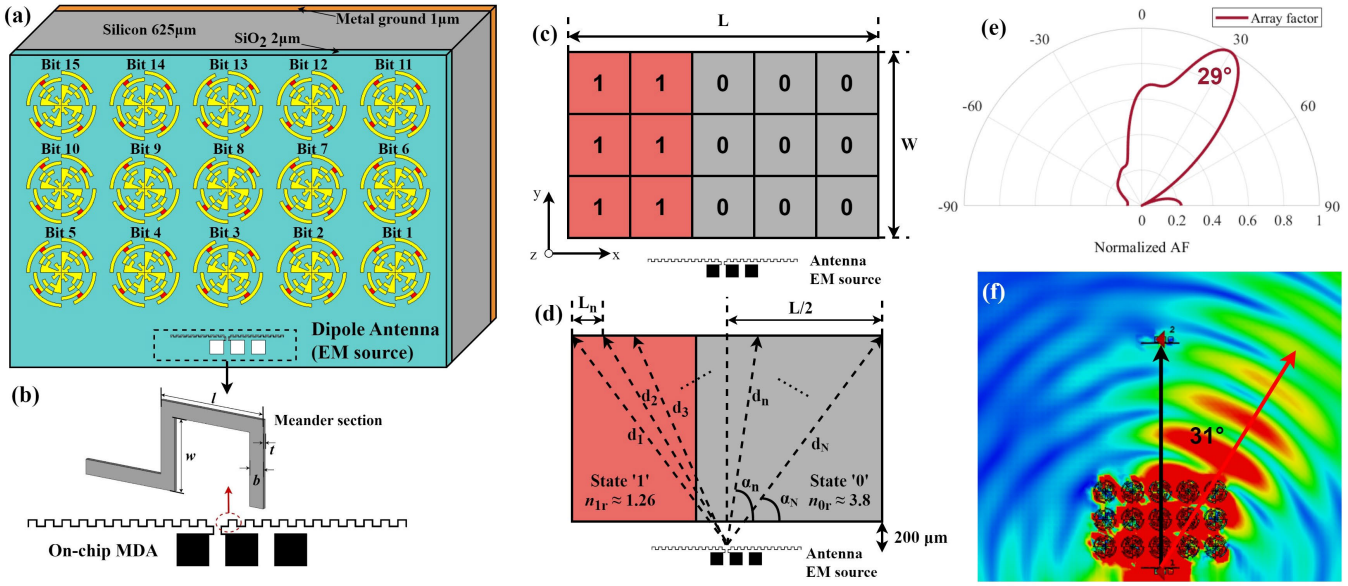

FIGURE 5. Design and analysis of the digital-coding metamaterial. (a) The layout of the digital-coding metamaterial is formed by a 3 × 5 array of binary coding unit cells and an on-chip meandering dipole antenna (MDA). (b) Structure layout and geometric parameters of the MDA. (c) Metamateiral with a binary coding of 110001100011000 and (d) its equivalent refractive index distribution, the route of EM rays inside two index mediums leads to different phase shifts. (e) The calculated array factor indicates the metamaterial can deflect the beam by 29°. (f) Simulated E-field distribution in CST indicates the main lobe of the dipole antenna is deflected by 31°.

of 100*100 μm and a pitch between two pads of 150 μm. Table 1 summarises the core performance parameters of the MDA operates at 70 GHz. The S_{11} of the MDA at 70 GHz is −22 dB. The −10 dB bandwidth of the antenna is around 15.48 GHz. The antenna exhibits low directivity and a wide radiation angle, consisting of two main lobes positioned at 0° and 180° direction with a maximum gain of 3.78 dBi and a 3 dB beamwidth of 102°. Similar on-chip MDAs have been widely used in many previous works as a standard broadcasting on-chip antenna [16], [18], given their compact size, simple structure, and easy fabrication.

The beam deflection analysis can be performed using the effective medium theory [20], where the substrate area containing states '0' and '1' unit cells can be approximated to uniform medium with complex refractive index $n_{0\mathrm{r}} + in_{0\mathrm{i}}$ and $n_{1\mathrm{r}} + in_{1\mathrm{i}}$. When the EM wave passes through a medium with an uneven refractive index distribution, the wave travels slower in regions with higher index and leads to deflection of the wavefront towards the direction with a higher effective index. Figure 5(c) provides an example of the metamaterial coded with a binary sequence of 110001100011000. The left two columns of the unit cells are set to state '1', which is marked in red with $n_{1\mathrm{r}} \approx 1.26$, and the three columns on the right are set to state '0' marked in grey with $n_{0\mathrm{r}} \approx 3.8$.

TABLE 1. Basic performance parameters of the 70GHz MDA.

Freq	70 GHz	Gain	3.78 dBi
S_{11} at 70 GHz	-22 dB	Efficiency	65%
Bandwidth (-10dB)	15.48 GHz	3 dB beamwidth	102°

The equivalent dielectric model and the EM path were labelled in Fig. 5(d). The L and W present the length and width of the metamaterial region. In our case, the diameter of the unit cell is 500 μm and the cell separation is 100 μm. The $L = 2900$ μm and $W = 1700$ μm. The on-chip dipole antenna is placed 200 μm below the metamaterial. To analyse the beam deflection angle, we can simplify the EM field radiating from the centre of the antenna into N number of EM rays, labelled as the black dotted arrows in Fig. 5(d). The n^{th} ray radiates from the EM source and enters the metamaterial with an angle α_n and travelled inside the metamaterial with a distance d_n:

$$\alpha_n = \tan^{-1}\left(\frac{w + 200 \times 10^{-6}}{|L/2 - nL_n|}\right), \tag{3a}$$

$$d_n = \frac{L}{\sin(\alpha_n)}, \tag{3b}$$

where L_n equals to $L/(N-1)$. It can be observed that each ray travels with a different distance in the state '0' and state '1' medium, which will lead to a different phase shift when leaving the metamaterial, the phase component of the n^{th} EM ray can be expressed as [46]:

$$\varphi_n = k_0 n_{0\mathrm{r}} d_{n0} + k_0 n_{1\mathrm{r}} d_{n1}, \tag{4}$$

where k_0 is the free space wavenumber, $n_{0\mathrm{r}}$ and $n_{1\mathrm{r}}$ are the effective refractive index of metamaterial under states '0' and '1', d_{n0} and d_{n1} are the path length of the n^{th} ray travelled in the state '0' and '1' medium respectively. Besides the phase shift, each ray will have a different amplitude component due to the different absorption coefficients. The amplitude

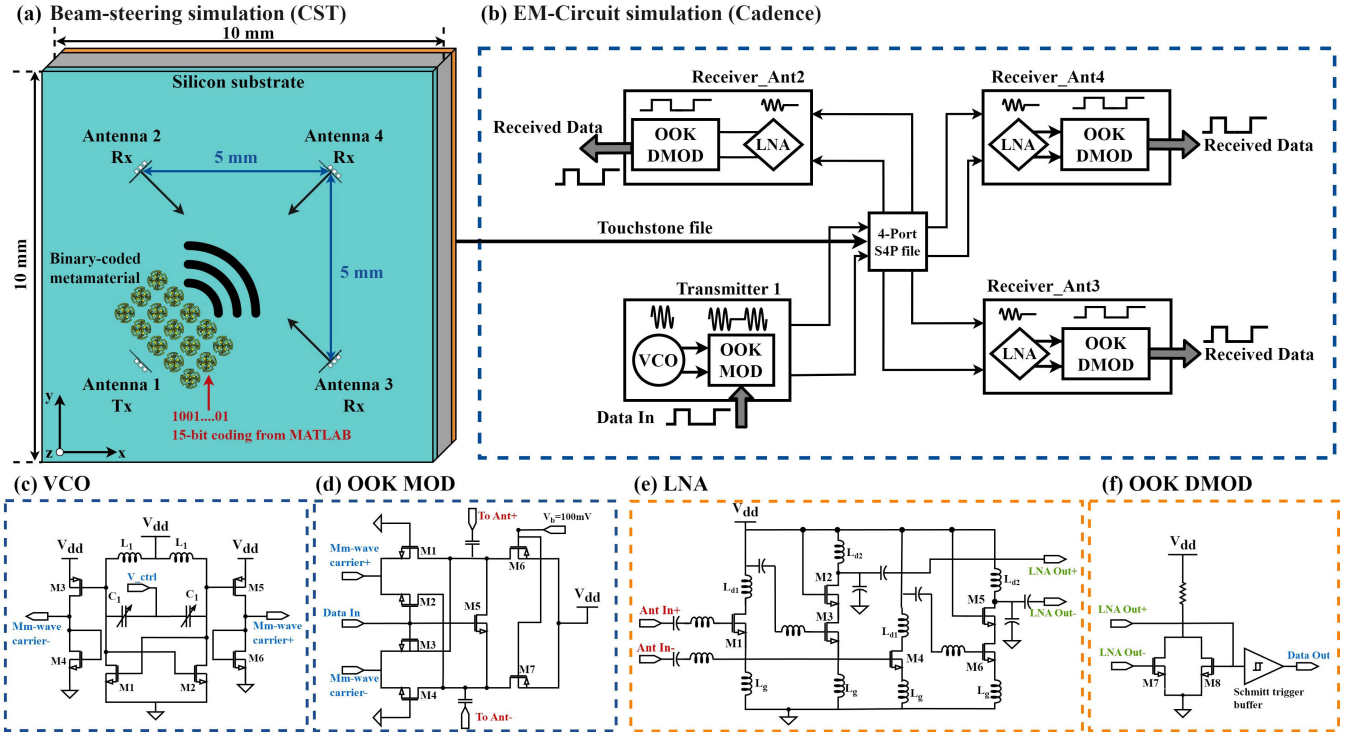

FIGURE 6. Simulation setup and circuit design for beamsteering and multi-mode transmission analysis. (a) Metamaterial beamsteering test with full-wave simulation based on a four-antenna intra-chip transmission setup, the metamaterial is placed in front of the transmitter antenna 1, and the other three antennas work as receivers. (b) Circuit setup to evaluate different transmission modes on the digital side consists of one wireless transmitter module connected to antenna 1 and three wireless receivers accepted signal from the antenna 2,3 and 4. Schematics diagram of the wireless transceiver circuit components with (c) Voltage-controlled oscillator (VCO) and (d) On-Off-Keying (OOK) modulator at the transmitter side. (e) Low-noise amplifier (LNA) and (f) OOK demodulator at the receiver side.

component of the n^{th} EM ray can be expressed as [59]:

$$A_n = e^{-k_0(n_{0i}d_{n0}+n_{1i}d_{n1})}. \tag{5}$$

After calculating the phase shift and amplitude component of all the EM rays, we can drive an n point phase distribution of EM wave on the top edge of the metamaterial array. We can approximate it into an equally spaced linear phased array with N radiation units and equal separation distance of L_n; the array factor can be calculated as [60]:

$$AF = \sum_{n=1}^{N} A_n e^{j(k_r n L_n \cos(\phi))+\varphi_n)}, \tag{6}$$

where k_r is the dielectric wavenumber inside the silicon substrate with $\varepsilon_r \approx 11.9$, A_n is the amplitude component of each radiation element. The phase component $k_r n L_n \cos(\phi) + \varphi_n$ will vary based on the angle of arrival ϕ, and the phase shift caused by the metamaterial φ_n is added to each radiation element. Figure 5(e) presents the calculated array factor plotted in the semi-polar coordinates. It can be observed that the main lobe of the antenna was deflected to the $+29°$ compared with the original main lobe pointing towards $0°$. The simulated E-field distribution in Fig. 5(f) clearly presents the deflection of the beam caused by the same metamaterial setup. The beam deflection angle can be measured around $31°$, which shows a good agreement with the calculation. In addition, the high absorption coefficient of the state 1 unit cells can attenuate the unwanted radiation outside the main lobe direction, which makes the proposed metamaterial exhibit a better side lobe suppression effect compared to previous beam deflection metamaterials [34]. This improvement helps to reduce the side lobe interference to the non-transmitting region during the beam deflection process.

IV. CIRCUIT DESIGN AND SIMULATION SETUP

A. SIMULATION SETUP

In this section, we explore the beam-steering capabilities of the digital-coding metamaterial through a series of electromagnetic (EM) and circuit simulations. Figure 6(a) illustrates the setup for the beam-steering simulation performed in CST: an intra-chip transmission system comprising four dipole antennas on a 10×10 mm silicon chip with a resistivity of $50\ \Omega \cdot$ m. The horizontal and vertical separation between the two adjacent dipoles is 5 mm, while the diagonal dipoles are separated by 7.07 mm. Each antenna is oriented with its main lobe directed towards the centre of the chip, as indicated by the small black arrows in Fig. 6(a). This arrangement maximises the transmission coverage of each dipole antenna. A similar antenna configuration has been widely used as a transmission benchmark in previous studies

[7], [13], [29], [50], which effectively emulates the wireless router placement in a mesh-based Wireless Network-on-Chip (WiNoC). The proposed digital-coding metamaterial is positioned in front of the transmitter (Tx) antenna 1 for on-chip beamsteering, while the remaining three antennas serve as wireless receivers (Rx). Each antenna has a 50-Ω lumped port applied across its GSG pad for S-parameter measurement. The transmission S-parameters from the Tx antenna 1 to the Rx antennas are recorded under each coding sequence, which are used as inputs for the next stage of EM-circuit co-simulation.

During the beam-steering analysis, MATLAB is used to input the 15-bit coding sequence to CST through the CST-MATLAB Interface, which changes the 15 pre-defined parameters that control the switching state of each unit cell in the CST. Different coding sequences will generate different radiation patterns and beam deflection angles, affecting the signal strength received by each Rx antenna. The proposed digital-coding metamaterial consists of 15 independent controlled unit cells that allow 32768 different coding sequences. However, not all sequences can generate radiation patterns that could contribute as a helpful transmission mode for the given intra-chip interconnects. A proper coding sequence can be selected through forward calculations and simulations or by inverse design. The forward design calculates the beam deflection angle caused by each refractive index distribution of the metamaterial and then verifies it through the simulation. The reverse design can be performed using a similar optimisation flow in Fig. 2(c) using the genetic algorithm when a specific design objective is known (Such as a particular beam deflection angle). For the existing 3×5 array, forward design is sufficient for some basic transmission modes, while reverse design can become more advantageous as the array size of the metamaterial is further expanded or more complex coding schemes are introduced.

The setup of EM-Circuit co-simulation is present in Fig. 6(b). The SPICE-level circuit simulation is performed using Cadence Virtuoso. The testing circuitry consists of one wireless transmitter module and three identical wireless receiver modules. All transceiver modules are connected to a 4-Port interface module provided by Cadence' analogLib', which reads the S4P touchstone file (S-parameter) output from the beam-steering simulation in CST. The transmitter module consists of a voltage-controlled oscillator (VCO) that generates the 70 GHz carrier wave. The transmitted data is modulated on the carrier wave using an On-Off-Keying modulator. Each Rx module contains a low-noise amplifier (LNA) to compensate for the transmission losses and a demodulator to recover the data from the modulated signal. The output from transmitter 1 is connected to the port 1 position, which corresponds to the Tx antenna 1. The three receiver modules are connected to the Rx antenna 2, 3 and 4, respectively. During EM-Circuit co-simulation, a 5 Gbps clock signal (Repeated 0 and 1) is modulated on the 70 GHz carrier wave and transmitted to the three receiver modules. The results from the beam-steering simulation will directly affect the received signal amplitude and which receiver modules can correctly decode the data.

B. WIRELESS TRANSCEIVER CIRCUIT DESIGN

Figure 6(c)-(f) provides the schematic diagrams of the transceiver circuit components. All circuit components are designed using TSMC 65 nm technology. The wireless transceiver adopts the On-Off-Keying (OOK) modulation scheme [3], [27]. A binary 1 represents the continuous transmission of the carrier wave during the logic period, and binary 0 represents no carrier wave (Amplitude = 0) being transmitted in the period.

The VCO presented in Fig. 6(c) generates the high-frequency carrier wave, which consists of an LC tank (L_1 and C_1) to provide the initial oscillation. Where C1 are voltage-controlled NMOS capacitors, their capacitance varies with the control voltage (V_{ctrl}), which changes the oscillation frequency of the LC tank. A cross-coupled NMOS pair (M1 and M2) to provide a unit gain and satisfy the Barkhausen criteria. The VCO outputs a differential carrier wave to the modulator. The OOK modulator in Fig. 6(d) adopted a leakage compensation design proposed in [18]. The two cross-coupled NMOS pairs (M1 and M3, M2 and M4) work as two leakage compensation groups. M2 and M3 receive the incoming digital signal to switch ON and OFF the carrier wave. M1 and M4 provide differential leakage drain current that is 180° out of phase to that of M2 and M3. The leaked currents of transistors will cancel each other out to improve the on-off isolation during modulation.

The first circuit component at the wireless receiver is the low-noise amplifier used to composite the transmission path loss from antenna 1 to the receiver antennas. Presented in Fig. 6(e), the LNA has two differential amplification stages connected in series: a common source stage (M1 and M4) with peak amplification around 66 GHz, followed by a second cascode stage (M2-M3 and M5-M6) amplifying at 75 GHz. The two states are amplifying on slightly different frequencies, which can compensate to form a wider 10 dB amplification bandwidth around 15 GHz and a maximum amplification gain of 24 dB. After amplification, the wireless signal is processed by the OOK demodulator, which consists of a NOMS rectifier transfer followed by a Schmitt trigger inverter. The rectifier (M1 and M2) transfers the differential input into an inverted single-ended envelope. The Schmitt trigger inverter circuit adjusts the duty ratio on the output square signal and buffers the output signal.

V. RESULT AND DISCUSSION

A. SIMULATION RESULTS

Figure 7 presents ten distinct transmission modes achieved by applying different coding sequences on the 3×5 digital-coding metamaterial, which can work as control presets for the antenna network to meet the typical transmission target requirements. The bottom left of each sub-figure depicts the configuration of the 3×5 unit cell array and the binary

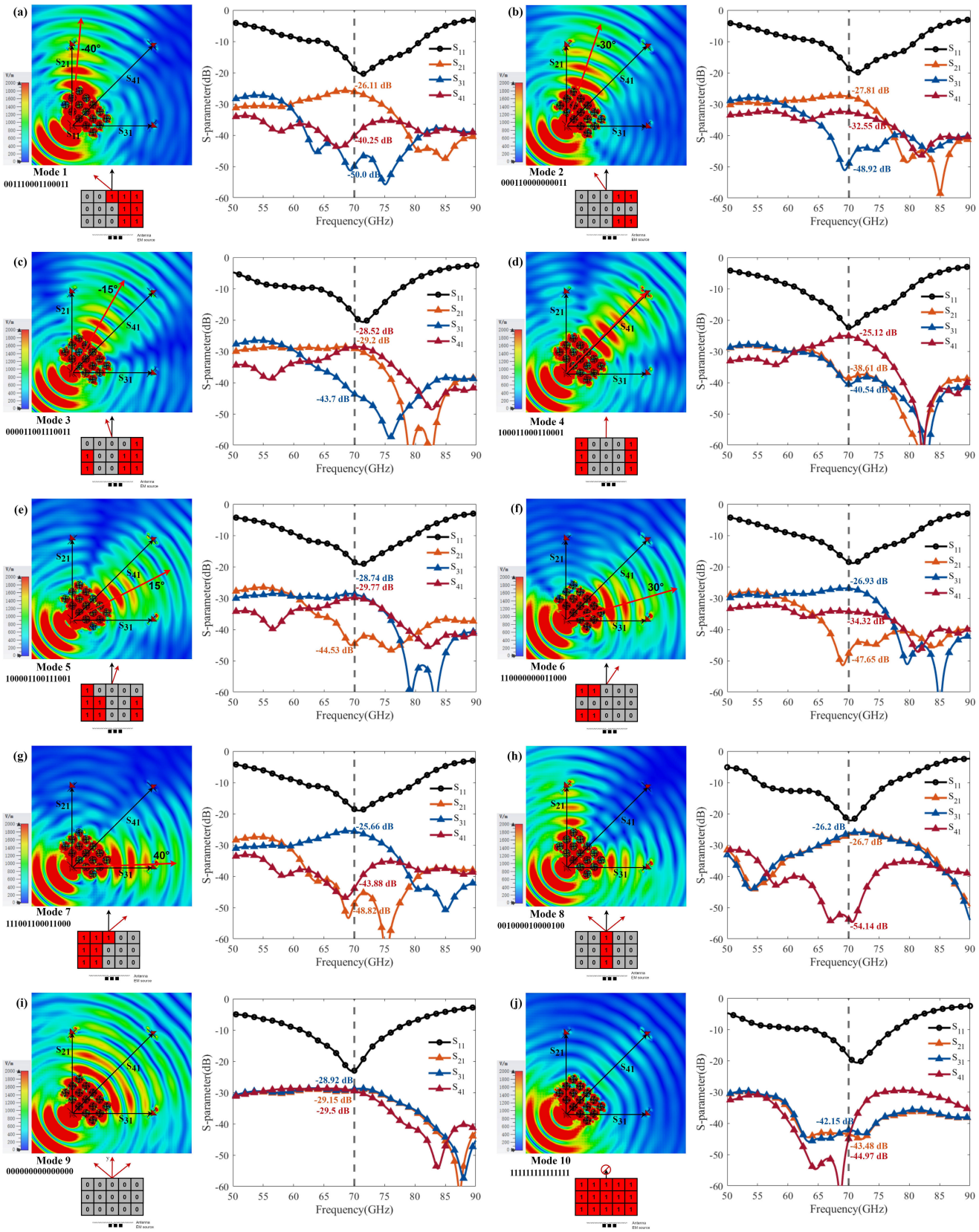

FIGURE 7. Ten presets of transmission modes achieved with different binary coding on the metamaterial. Including (a) −40°, (b) −30°, (c) −15°, (d) 0°, (e) +15°, (f) +30°, (g) +40° beam deflection. (h) Beam splitting, (i) broadcasting and (j) attenuation modes. Each image provides the binary coding sequence, state map, the simulated electric field distribution across the chip and S-parameters under each mode. The S_{11} represent return loss at antenna 1, and S_{21}, S_{31}, and S_{41} represent the transmission coefficient from antenna 1 to three receiver antennas.

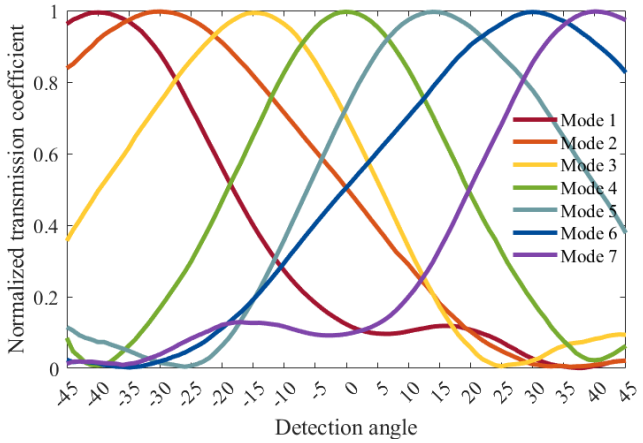

FIGURE 8. Normalised transmission magnitude at 70 GHz versus the detection angle from −45° to +45° under mode 1 to mode 7.

sequence that enables the transmission mode. The upper left of each sub-figure shows the electric field distribution within the silicon chip, with the black arrow indicating the direction of the main lobe of antenna 1 and the red arrow indicating the beam direction after deflection by the metamaterial. The right side of each sub-figure presents the simulated S-parameters of the four antennas labelled from S_{11} to S_{41}. The S_{11} represent the return loss of the Tx antenna 1, and the S_{21}, S_{31}, and S_{41} are the transmission coefficients, indicating how much percentage of power is delivered to each Rx across the chip from the antenna 1. Under a baseline transmission case without the metamaterial, the S_{21}, S_{31}, and S_{41} are simulated as −31.06 dB, −30.9 dB, and −28.43 dB at 70 GHz, which are main contributed by the path loss and the dielectric loss from the silicon substrate.

Figures 7(a) to 7(g) display seven different beamsteering angles achieved by the metamaterial, ranging from −40° to +40°. Modes 1 and 7 exhibit the largest deflection range achievable by the metamaterial, where the state '0' and '1' unit cells each occupy around half of the metamaterial. In Mode 1, the beam of the on-chip dipole is strongly deflected by approximately −40° (anti-clockwise) towards antenna 2. The S_{21} value receives a 4.95 dB enhancement at 70 GHz compared with a broadcasting transmission without the metamaterial, while the S_{21} and S_{31} are noticeably attenuated to −40 to −50 dB. Modes 2 and 3 gradually reduce the beam deflection angle to −30° and −15°. In this process, antenna four is gradually incorporated into the radiation area of the antenna lobe. At −15° deflection angle, the S_{21} and S_{31} are both located around −29 dB and with an additional −15 dB channel separation with the antenna 3.

Figure. 7(d) presents the transmission mode 4 with a zero-degree beam deflection angle. The state distribution of the unit cells in the metamaterial is centre-symmetrical. Three columns of state '0' unit cells with a higher index were arranged in the middle, flanked by state '1' unit cells with a lower index on either side. This arrangement can work as a metamaterial lens, narrowing the beam width of the dipole antenna and enhancing transmission gain. The S_{41} under mode 4 at 70 GHz is improved by 3.3 dB compared with a broadcasting transmission, which means that the signal strength received at antenna 4 is doubled. Mode 5 to mode 7 shows positive beam deflection angles (Clockwise) from +15° to +40° towards the antenna 3. Figure 8 presents the normalised radiation pattern under a detection angle of ± 45° at 70 GHz, which clearly presents the beam-steering range under each transmission mode from −40° to +40° in mode 1 to mode 7. It is important to note that Fig. 7 does not display all the possible beam-steering modes that can be supported by 3 × 5 digital-coding metamaterial. During simulation verification, the metamaterial can achieve a beam-steering range from −40° to +40° with a minimum step size around 5°.

The metamaterial in mode 8 also features a center-symmetric configuration but with a column of state '1' unit cells in the middle and state '0' unit cells on both sides. This setup acts as a 90° beam splitter, equally dividing the beam into two parts directed towards −45° and +45° directions to the antenna 2 and 3.

Modes 9 and 10 present two special cases where all unit cells are in the same state, resulting in an evenly distributed refractive index within the metamaterial. In mode 9, with all unit cells in state '0', the dipole antenna maintains its original radiation pattern, broadcasting the signal to all three antennas. In mode 10, with all unit cells in state '1', the higher imaginary part (1.08) of the refractive index leads to a significant signal attenuation when the EM wave passes through three layers of unit cells. This functionality can be particularly useful on a larger chip involving more transmitter and receive antennas. The metamaterial can 'switch off' half of the main lobe of the dipole antenna, thereby reducing interference to other regions of the chip.

Figure 9 presents the results of the EM-circuit simulation under the ten transmission modes. It displays the output waveforms of the three receiver modules at antennas 2, 3, and 4. The top line of each subfigure plots the amplified signal from the low-noise amplifiers (LNAs), and the bottom line shows the demodulated signal at the on-off keying (OOK) demodulator. This test demonstrates that through active beam control, the digital-coding metamaterials can accurately select transmission targets and enable data transmission among multiple receivers without the need for any transmission identification codes or medium access control protocols.

The data transmission conditions can be classified into four categories based on the number of receivers that successfully decoded the data. The first category comprises modes 1, 4, and 7, shown in Figs. 9(a), 9(d), and 9(g). The data (clock signal) is successfully delivered to a specific antenna with a directional point-to-point transmission. The signals received by the other two antennas are significantly attenuated and cannot be decoded even after proper amplification. The second category includes modes 3, 5, and 8, illustrated in Figs. 9(c), 9(e), and 9(h). In these modes, the data is

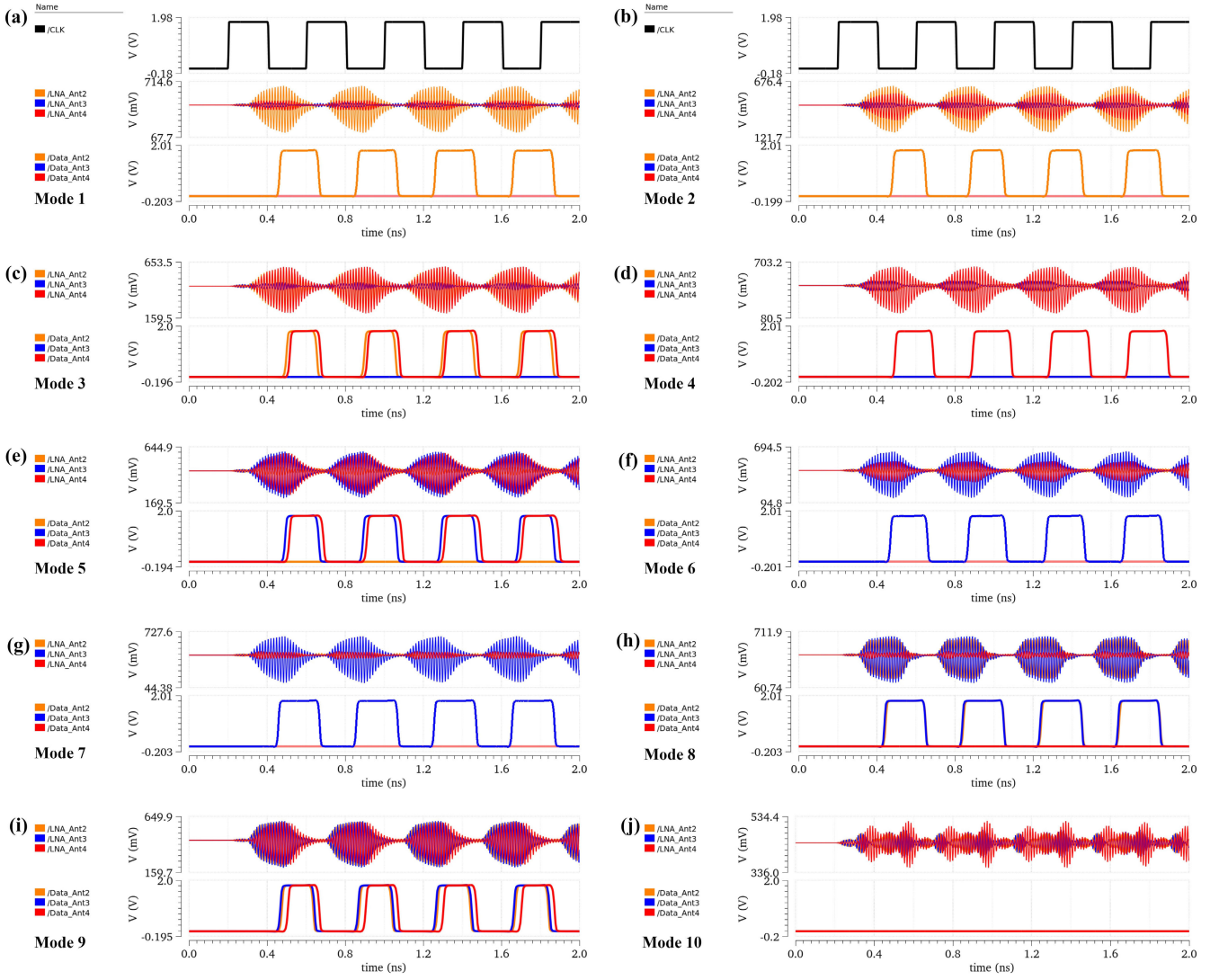

FIGURE 9. Data waveform at the LNA and data output in Fig. 6(b) under the 10 transmission modes. (a) Mode 1 with −40° beam deflection angle, only antenna 2 received the data. (b) Mode 2 with a −30° deflection angle, antenna 2 receives the data, but a noticeably higher amplitude is output by the antenna 4 LNA. (c) Mode 3 with a −15° deflection angle, both antenna 2 and 4 receive the data. (d) Mode 4 has a 0° directional transmission, and only antenna 4 receives the data. (e) Mode 5 with a +15° deflection angle, both antenna 3 and 4 receive the data. (e) Mode 6 with a +30° deflection angle, antenna 3 receives the data. (f) Mode 7 with a +40° deflection angle, antenna 3 receives the data. (f) Mode 8 with a 90° beam splitting transmission, antennas 2 and 3 receive the data. (l) Broadcasting transmission under mode 9, all three antennas receive the data. (j) Mode 10 works as a signal attenuator and none of the three antennas receive the data.

delivered to two selected antennas simultaneously using a less directional beam and smaller deflection angle in modes 3 and 5 or a 90° split beam in mode 8. The third category consists of mode 9 in Fig. 9(i), where the signal is broadcast to all three antennas, and all receiver modules can simultaneously decode the transmitted signal. Due to the longer transmission path to antenna 4, the received signal experiences a 0.03 ns delay compared to the signals received by the other two antennas. The last category consists of mode 10 in Fig. 9(j), where the signal is heavily attenuated and absorbed under this mode, and no receiver can demodulate the data. These results demonstrate the versatility and effectiveness of the digital-coding metamaterial in dynamically controlling signal distribution, providing targeted transmission or broad coverage as required.

B. SIMULTANEOUSLY TRANSMISSION

The results in Figs. 7 and 9 showcase the variable transmission modes achieved with a single digital-coding metamaterial. Its potential can be further expanded through the cooperation of multiple sets of these metamaterials on the same chip. Figure 10 presents a few cases incorporated with multiple digital-coding metamaterials enhanced transmitter antennas, similar to the schematic diagram provided in Fig. 1(c). The placement of the antenna and metamaterial remains the same, and the reconfiguration of interconnects

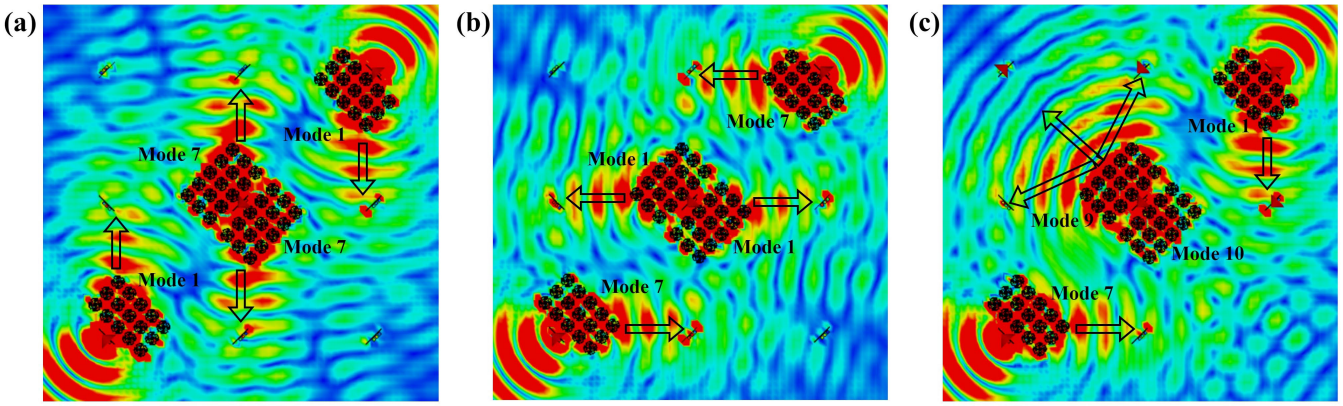

FIGURE 10. Illustrative examples of simultaneous transmission using multiple integrated digital-coding metamaterials on the same chip, featuring precise beam steering to prevent radiation overlap. (a) Three vertically arranged directional interconnects. (b) Three horizontally arranged directional interconnects. (c) Direction and broadcasting transmission to different areas of the chip simultaneously.

is fully achieved by changing the binary coding on each metamaterial. Figures 10(a) and 10(b) showcase the 'directional' interconnect using the metamateiral in vertical and horizontal directions. Three non-interfering transmissions can be performed on the same chip with directional beamsteering. Additionally, the directional interconnect can be reconfigured horizontally or vertically, which is hardly achieved by conventional high-directional antennas without beamsteering capabilities. Figure 10(c) demonstrates the configuration of broadcasting transmission and directional transmission on the same chip. The transmitter antenna broadcasts signals to multiple receivers on the top left part of the chip. The metamaterial under mode 10 absorbs the unwanted radiation from the on-chip dipole. The rest of the chip can be fully utilised for additional highly directional transmissions.

C. COMPARISON AND FURTHER WORK

Table 2 summarises and compares the existing on-chip beamforming approaches for intra and inter-chip wireless interconnects. Previous works focus on on-chip phased array antennas as the method for beam formation and steering, formed by two or four smaller on-chip antenna units and driving with an independent phase-shifting circuit. Work [24] and [25] provide two phased array designs based on omnidirectional patch antennas. When the antenna is fed with a quadrature (90°) phase shifting circuit, the antenna can achieve a full 360° scan of the main beam with a minimum step size of 90° [21]. However, the combination of four patch antennas results in a very large device area of more than 10 mm^2. Work [29] presents a more compact on-chip phased array using four zigzag monopole antennas and a passive feed system. The antenna can achieve three different radiation modes: broadside, phased and endfire by applying different feed systems, which cover a steering range of around 90°. However, the use of a passive phase-shifting system makes the antenna temporarily unavailable for dynamic beamsteering.

TABLE 2. Comparison of on-chip beam-steering approaches for intra-chip and inter-chip transmission.

Work	[29]	[25]	[24]	[22]	This work
Approach	Zigzag phased array	Patch phased array	Patch phased array	Phased array	Digital-coding metamaterial
Freq. (GHz)	60	60	60	60	70
Device area (mm^2)	2.4	28.3	13.40	Not given	4.93
Max. Steering range	90°	227°	360°	180°	80°(±40°)
Steering step size	Not given	90°	90°	90°	5°
Modes	3	4	4	8	≥10

Compared to previous on-chip beamforming solutions based on phased array antennas, the proposed on-chip digital-coding metamaterial offers superior beam control precision, with a beamsteering step size of approximately 5° and over 10 radiation modes to accommodate various on-chip transmission requirements. A single metamaterial can support a maximum beamsteering range of around 80°. However, it can be further extended to nearly 180° using two independent modules on the same antenna, as illustrated in the centre antenna of Fig. 9. Another advantage of the proposed digital-coding metamaterials is that it can be fully digitally controlled. Unlike phased array antennas, which require analogue phase-shifting circuits and complex feeding networks, the proposed metamaterial can be controlled by changing the switching state of the diodes in a fully digital manner, which can be supported by simpler control circuits and stronger immunity to interference and noise. The digital control function can be smoothly integrated with the wireless transceiver circuitry or the router circuitry in

WiNoC, which allows automatic configuration of the most optimal transmission mode according to the transmission target requirements.

TABLE 3. Size of the unit cell array versus beamsteering capability.

Array size	2x3	2x4	3x4	3x5	3x6
No. control bits	6	8	12	15	18
Area overhead (mm^2)	1.87	2.53	3.91	4.93	5.95
Max. Steering range	±32°	±35°	±38°	±40°	±46°
Steering step size	15°	10°	5°	5°	5°

The primary limitation of digital-coding unit cell arrays lies in their area overhead. The 3 × 5 unit cell array introduced in this study occupies an area of 4.93 mm^2 when operating at 70 GHz. Deploying multiple unit cell arrays on the same silicon chip will consume a considerable design space on the metal interconnect layer, making it more suitable for implementation within silicon interposers or dedicated transmission layers through three-dimensional integration with the circuit layer [7], [18]. As the frequency continues to grow, the footprint of individual unit cells and the metamaterial can be significantly reduced. The latest reported samples have realised on-chip antennas and transmitters up to 150 GHz [48], while the cut-off frequency of existing CMOS technology could theoretically support millimeter-wave interconnects up to 200 GHz [28], [49]. At these higher frequencies, the area required by the metamaterial can be reduced by a factor of 8 to 10 compared to 70 GHz designs.

Shrinking the metamaterial footprint by reducing the number of unit cells is feasible, but it comes with the sacrifice of beam control capability. Table 3 lists the size of the unit cell array versus the beam-steering capability, including maximum beam-steering range and steering step size. As the array size increases, more unit cells can provide a larger beamsteering angle and more precise steering. However, even the smallest arrays in the table can still provide a beam scanning range greater than 60°. In applications where the scanning accuracy is not critical, a smaller array can still noticeably enhance the beam control of on-chip antennas.

Area reduction can also be achieved by expanding the unit cell function. For instance, a multi-bit coding unit cell can further expand the control freedom of the refractive distribution. The one-bit coding unit cell discussed in Chapter II defines a single tunable pixel and two operation states when all transistors switch 'ON' or 'OFF' simultaneously. The proposed topological unit cell can be easily expanded into multi-bit coding by introducing more tunable pixels or more operating states when four diodes are partially switched 'ON'. This would allow for more refined refractive index distributions, leading to better beam control accuracy and a wider steering range with fewer unit cells than current one-bit coding metamaterials.

VI. CONCLUSION

We demonstrate a digital-coding metamaterial that enhances the beam-steering capability of on-chip antennas and enables multiple reconfigurable intra-chip transmission modes, paving the way for high-performance on-chip millimetre-wave interconnects. The unit cells of the metamaterial are topologically optimised for angle-independent resonance performance through a genetic algorithm. Each unit cell is independently tunable through on-chip SOI PIN diodes between two states with a refractive index of 3.8 and 1.26 at 70 GHz. The proposed metamaterial is formed by a 3×5 array of unit cells, which can be fully controlled through a 15-bit binary coding sequence that can change the refractive index distribution of the metamaterial to achieve different beam-steering angles and radiation patterns. We designed ten transmission presets for the metamaterial containing multiple functions, including adjustable beamsteering from −40° to +40°, transmission gain enhancement for 3.3 dB, 90° beam splitter, and signal attenuator. These transmission modes can be effectively applied for applications like improving transmission efficiency, multiple access control, and interference reduction, and they can be reconfigured according to the transmission requirements. Overall, our proposed digital-coding metamaterials can greatly enhance the flexibility of on-chip millimetre-wave transmission and can potentially serve as a standard design module for future on-chip wireless transmission protocols and wireless Network-on-Chip architectures.

REFERENCES

[1] Y. P. Zhang, Z. M. Chen, and M. Sun, "Propagation mechanisms of radio waves over intra-chip channels with integrated antennas: Frequency-domain measurements and time-domain analysis," *IEEE Trans. Antennas Propag.*, vol. 55, no. 10, pp. 2900–2906, Oct. 2007.

[2] S. Deb, A. Ganguly, P. P. Pande, B. Belzer, and D. Heo, "Wireless NoC as interconnection backbone for multicore chips: Promises and challenges," *IEEE J. Emerg. Sel. Topics Circuits Syst.*, vol. 2, no. 2, pp. 228–239, Jun. 2012.

[3] K. Chang, S. Deb, A. Ganguly, X. Yu, S. P. Sah, P. P. Pande, B. Belzer, and D. Heo, "Performance evaluation and design trade-offs for wireless network-on-chip architectures," *ACM J. Emerg. Technol. Comput. Syst.*, vol. 8, no. 3, pp. 1–25, Aug. 2012.

[4] X. Yu, J. Baylon, P. Wettin, D. Heo, P. P. Pande, and S. Mirabbasi, "Architecture and design of multichannel millimeter-wave wireless NoC," *IEEE Des. Test*, vol. 31, no. 6, pp. 19–28, Dec. 2014.

[5] S. Deb, A. Ganguly, K. Chang, P. Pande, B. Beizer, and D. Heo, "Enhancing performance of network-on-chip architectures with millimeter-wave wireless interconnects," in *Proc. 21st IEEE Int. Conf. Appl.-specific Syst., Archit. Processors (ASAP)*, Jul. 2010, pp. 73–80.

[6] M. Sun, Y. P. Zhang, G. X. Zheng, and W.-Y. Yin, "Performance of intra-chip wireless interconnect using on-chip antennas and UWB radios," *IEEE Trans. Antennas Propag.*, vol. 57, no. 9, pp. 2756–2762, Sep. 2009.

[7] I. El Masri, T. Le Gouguec, P.-M. Martin, R. Allanic, and C. Quendo, "Electromagnetic characterization of the intrachip propagation channel in *Ka* -and *V* -bands," *IEEE Trans. Compon., Packag., Manuf. Technol.*, vol. 9, no. 10, pp. 1931–1941, Oct. 2019.

[8] H. K. Mondal, S. H. Gade, M. S. Shamim, S. Deb, and A. Ganguly, "Interference-aware wireless network-on-chip architecture using directional antennas," *IEEE Trans. Multi-Scale Comput. Syst.*, vol. 3, no. 3, pp. 193–205, Jul. 2017.

[9] M. S. Shamim, N. Mansoor, A. Samaiyar, A. Ganguly, S. Deb, and S. S. Ram, "Energy-efficient wireless network-on-chip architecture with log-periodic on-chip antennas," in *Proc. 24th, Ed., Great Lakes Symp. VLSI (GLSVLSI)*, New York, NY, USA, 2014, pp. 85–86.

[10] Y. P. Zhang, M. Sun, and L. H. Guo, "On-chip antennas for 60-GHz radios in silicon technology," *IEEE Trans. Electron Devices*, vol. 52, no. 7, pp. 1664–1668, Jul. 2005.

[11] S. Adamshick, A. Johnson, K. Moriarty, W. Tremblay, and J. Burke, "Antenna on chip design utilizing 3D integration for mixed signal applications," in *Proc. IEEE 60th Int. Midwest Symp. Circuits Syst. (MWSCAS)*, Aug. 2017, pp. 209–212.

[12] R. Karim, A. Iftikhar, B. Ijaz, and I. Ben Mabrouk, "The potentials, challenges, and future directions of on-chip-antennas for emerging wireless applications—A comprehensive survey," *IEEE Access*, vol. 7, pp. 173897–173934, 2019.

[13] R. S. Narde, J. Venkataraman, A. Ganguly, and I. Puchades, "Intra- and inter-chip transmission of millimeter-wave interconnects in NoC-based multi-chip systems," *IEEE Access*, vol. 7, pp. 112200–112215, 2019.

[14] B. Floyd, C.-M. Hung, and K. O. Kenneth, "A 15-GHz wireless interconnect implemented in a 0.18-μm CMOS technology using integrated transmitters, receivers, and antennas," *IEEE J. Solid-State Circuits*, vol. 37, no. 5, pp. 543–552, May 2002.

[15] W. Moriyama, S. Kubota, K. Kimoto, N. Sasaki, and T. Kikkawa, "On-chip Micro-meander-antennas for silicon LSI wireless interconnects," in *Proc. IEEE Antennas Propag. Soc. Int. Symp.*, Jul. 2008, pp. 1–4.

[16] K. O. Kenneth et al., "On-chip antennas in silicon ICs and their application," *IEEE Trans. Electron Devices*, vol. 52, no. 7, pp. 1312–1323, Jul. 2005.

[17] V. Pano, Y. Liu, I. Yilmaz, A. More, B. Taskin, and K. Dandekar, "Wireless NoCs using directional and substrate propagation antennas," in *Proc. IEEE Comput. Soc. Annu. Symp. VLSI (ISVLSI)*, Jul. 2017, pp. 188–193.

[18] Q. Ding, G. Knight, and T. Mak, "An active silicon interposer with low-power hybrid wireless-wired clock distribution network for many-core systems," *IEEE Trans. Very Large Scale Integr. (VLSI) Syst.*, vol. 28, no. 9, pp. 2042–2054, Sep. 2020.

[19] Q. Ding, B. J. Fletcher, and T. Mak, "Globally wireless locally wired (GloWiLoW): A clock distribution network for many-core systems," in *Proc. IEEE Int. Symp. Circuits Syst. (ISCAS)*, May 2018, pp. 1–5.

[20] D. R. Smith, D. C. Vier, T. Koschny, and C. M. Soukoulis, "Electromagnetic parameter retrieval from inhomogeneous metamaterials," *Phys. Rev. E, Stat. Phys. Plasmas Fluids Relat. Interdiscip. Top.*, vol. 71, no. 3, pp. 1–11, Mar. 2005.

[21] P. Baniya and K. L. Melde, "Switched-beam endfire planar array with integrated 2-D Butler matrix for 60 GHz chip-to-chip space-surface wave communications," *IEEE Antennas Wireless Propag. Lett.*, vol. 18, pp. 236–240, 2019.

[22] S. Abadal, A. Marruedo, A. Franques, H. Taghvaee, A. Cabellos-Aparicio, J. Zhou, J. Torrellas, and E. Alarcón, "Opportunistic beamforming in wireless Network-on-Chip," in *Proc. IEEE Int. Symp. Circuits Syst. (ISCAS)*, Sapporo, Japan, May 2019, pp. 1–5.

[23] M.-A. Chung, Y.-H. Chen, and I.-P. Meiy, "Antenna-on-chip for millimeter wave applications using CMOS process technology," *Telecom*, vol. 4, no. 1, pp. 146–164, Feb. 2023.

[24] P. Baniya, A. Bisognin, K. L. Melde, and C. Luxey, "Chip-to-chip switched beam 60 GHz circular patch planar antenna array and pattern considerations," *IEEE Trans. Antennas Propag.*, vol. 66, no. 4, pp. 1776–1787, Apr. 2018.

[25] P. Baniya, S. Yoo, K. L. Melde, A. Bisognin, and C. Luxey, "Switched-beam 60-GHz four-element array for multichip multicore system," *IEEE Trans. Compon., Packag., Manuf. Technol.*, vol. 8, no. 2, pp. 251–260, Feb. 2018.

[26] W. Yang, K. Ma, K. S. Yeo, and W. M. Lim, "A 60 GHz on-chip antenna in standard CMOS silicon technology," in *Proc. IEEE Asia–Pacific Conf. Circuits Syst.*, Dec. 2012, pp. 252–255.

[27] A. Ganguly, M. Ahmed, R. Singh Narde, A. Vashist, M. Shamim, N. Mansoor, T. Shinde, S. Subramaniam, S. Saxena, J. Venkataraman, and M. Indovina, "The advances, challenges and future possibilities of millimeter-wave chip-to-chip interconnections for multi-chip systems," *J. Low Power Electron. Appl.*, vol. 8, no. 1, p. 5, Feb. 2018.

[28] T. Kikkawa, P. Kanai Saha, N. Sasaki, and K. Kimoto, "Gaussian monocycle pulse transmitter using 0.18 μm CMOS technology with on-chip integrated antennas for inter-chip UWB communication," *IEEE J. Solid-State Circuits*, vol. 43, no. 5, pp. 1303–1312, May 2008.

[29] R. S. Narde, J. Venkataraman, A. Ganguly, and I. Puchades, "Antenna arrays as millimeter-wave wireless interconnects in multichip systems," *IEEE Antennas Wireless Propag. Lett.*, vol. 19, pp. 1973–1977, 2020.

[30] H. F. Ma, X. Chen, H. S. Xu, X. M. Yang, W. X. Jiang, and T. J. Cui, "Experiments on high-performance beam-scanning antennas made of gradient-index metamaterials," *Appl. Phys. Lett.*, vol. 95, no. 9, pp. 93–96, Aug. 2009.

[31] A. Dadgarpour, B. Zarghooni, B. S. Virdee, and T. A. Denidni, "One- and two-dimensional beam-switching antenna for millimeter-wave MIMO applications," *IEEE Trans. Antennas Propag.*, vol. 64, no. 2, pp. 564–573, Feb. 2016.

[32] B. A. F. Esmail, H. B. Majid, S. H. Dahlan, Z. Z. Abidin, M. K. A. Rahim, and M. Jusoh, "Planar antenna beam deflection using low-loss metamaterial for future 5G applications," *Int. J. RF Microw. Comput.-Aided Eng.*, vol. 29, no. 10, Jun. 2019, Art. no. e21867.

[33] B. A. F. Esmail, M. K. A. Rahim, H. A. Majid, N. A. Murad, N. A. Samsuri, O. Ayop, A. Salh, and N. Al-Fadhali, "Deflected beam pattern through reconfigurable metamaterialstructure at 3.5 GHz for 5G applications," *Waves Random Complex Media*, pp. 1–24, Mar. 2022, doi: 10.1080/17455030.2022.2053608.

[34] B. A. Esmail, H. Majid, Z. Z. Abidin, S. H. Dahlan, M. Himdi, R. Dewan, M. K. A. Rahim, and N. Al-Fadhali, "Reconfigurable radiation pattern of planar antenna using metamaterial for 5G applications," *Materials*, vol. 13, no. 3, p. 582, Jan. 2020.

[35] H.-X. Xu, G.-M. Wang, Z. Tao, and T. J. Cui, "High-directivity emissions with flexible beam numbers and beam directions using gradient-refractive-index fractal metamaterial," *Sci. Rep.*, vol. 4, no. 1, p. 5744, Jul. 2014.

[36] T. J. Cui, M. Q. Qi, X. Wan, J. Zhao, and Q. Cheng, "Coding metamaterials, digital metamaterials and programmable metamaterials," *Light, Sci. Appl.*, vol. 3, no. 10, p. e218, Oct. 2014.

[37] L. Zhang, X. Q. Chen, S. Liu, Q. Zhang, J. Zhao, J. Y. Dai, G. D. Bai, X. Wan, Q. Cheng, G. Castaldi, V. Galdi, and T. J. Cui, "Space-time-coding digital metasurfaces," *Nature Commun.*, vol. 9, no. 1, p. 4334, Oct. 2018.

[38] F. Yang, F. Xu, C. Liu, X. Yang, Z. Wang, J. Wu, and X. Fu, "Two-dimensional beam steering based on compact programmable coding metasurface," *Appl. Sci.*, vol. 12, no. 22, p. 11780, Nov. 2022.

[39] S. Taravati and G. V. Eleftheriades, "Full-duplex reflective beamsteering metasurface featuring magnetless nonreciprocal amplification," *Nature Commun.*, vol. 12, no. 1, p. 4414, Jul. 2021.

[40] C. Huang, B. Sun, W. Pan, J. Cui, X. Wu, and X. Luo, "Dynamical beam manipulation based on 2-bit digitally-controlled coding metasurface," *Sci. Rep.*, vol. 7, no. 1, p. 42302, Feb. 2017.

[41] K. W. Cho, M. H. Mazaheri, J. Gummeson, O. Abari, and K. Jamieson, "MmWall: A reconfigurable metamaterial surface for mmWave networks," in *Proc. 22nd Int. Workshop Mobile Comput. Syst. Appl.*, Feb. 2021, pp. 119–125.

[42] W. Withayachumnankul, C. Fumeaux, and D. Abbott, "Compact electric-LC resonators for metamaterials," *Opt. Exp.*, vol. 18, no. 25, p. 25912, Nov. 2010.

[43] S. Kumar, A. Kumari, and B. Pradhan, "Analysis of evanescent field of TE and TM mode in the grounded slab metamaterial waveguide structure," *Optik*, vol. 126, no. 23, pp. 3706–3712, Dec. 2015.

[44] L. Li, T. Jun Cui, W. Ji, S. Liu, J. Ding, X. Wan, Y. Bo Li, M. Jiang, C.-W. Qiu, and S. Zhang, "Electromagnetic reprogrammable coding-metasurface holograms," *Nature Commun.*, vol. 8, no. 1, p. 197, Aug. 2017.

[45] Q. Ma, C. B. Shi, G. D. Bai, T. Y. Chen, A. Noor, and T. J. Cui "Beam-editing coding metasurfaces based on polarisation bit," *Adv. Opt. Mater.*, vol. 5, no. 23, Sep. 2017, Art. no. 1700548.

[46] B. A. F. Esmail, S. Koziel, L. Golunski, H. B. A. Majid, and R. K. Barik, "Overview of metamaterials-integrated antennas for beam manipulation applications: The two decades of progress," *IEEE Access*, vol. 10, pp. 67096–67116, 2022.

[47] Q. Ma, G. D. Bai, H. B. Jing, C. Yang, L. Li, and T. J. Cui, "Smart metasurface with self-adaptively reprogrammable functions," *Light, Sci. Appl.*, vol. 8, no. 1, p. 98, Oct. 2019.

[48] T. Kuwabara, N. Oshima, K. Tanji, N. Tawa, S. Hachiyama, and T. Kaneko, "D-band 4-ch Antenna-on-chip phased-array TX front-end," in *Proc. IEEE BiCMOS Compound Semiconductor Integr. Circuits Technol. Symp. (BCICTS)*, Oct. 2023, pp. 183–186.

[49] B. Khamaisi, S. Jameson, and E. Socher, "A 210–227 GHz transmitter with integrated on-chip antenna in 90 nm CMOS technology," *IEEE Trans. Terahertz Sci. Technol.*, vol. 3, no. 2, pp. 141–150, Mar. 2013.

[50] M. S. Shamim, N. Mansoor, R. S. Narde, V. Kothandapani, A. Ganguly, and J. Venkataraman, "A wireless interconnection framework for seamless inter and intra-chip communication in multichip systems," *IEEE Trans. Comput.*, vol. 66, no. 3, pp. 389–402, Mar. 2017.
[51] S. Taravati and G. V. Eleftheriades, "Full-duplex nonreciprocal beam steering by time-modulated phase-gradient metasurfaces," *Phys. Rev. Appl.*, vol. 14, no. 1, Jul. 2020, Art. no. 014027.
[52] R. Karimian, S. Taravati, M. D. Ardakani, S. Ahmadi, and M. E. Zaghloul, "Nonreciprocal-beam phased-array antennas based on transistor-loaded phase shifters," *IEEE Trans. Antennas Propag.*, vol. 69, no. 11, pp. 7572–7581, Nov. 2021.
[53] S. Taravati and A. A. Kishk, "Advanced wave engineering via obliquely illuminated space-time-modulated slab," *IEEE Trans. Antennas Propag.*, vol. 67, no. 1, pp. 270–281, Jan. 2019.
[54] P. Y. Chen, C. H. Chen, H. Wang, J. H. Tsai, and W. X. Ni, "Synthesis design of artificial magnetic metamaterials using a genetic algorithm," *Opt. Exp.*, vol. 16, no. 17, p. 12806, Aug. 2008.
[55] P. Min, Z. Song, L. Yang, V. G. Ralchenko, and J. Zhu, "Optically transparent flexible broadband metamaterial absorber based on topology optimization design," *Micromachines*, vol. 12, no. 11, p. 1419, Nov. 2021.
[56] S. Sui, H. Ma, J. Wang, Y. Pang, and S. Qu, "Topology optimization design of a lightweight ultra-broadband wide-angle resistance frequency selective surface absorber," *J. Phys. D, Appl. Phys.*, vol. 48, no. 21, Apr. 2015, Art. no. 215101.
[57] M. Nedeljkovic, C. G. Littlejohns, A. Z. Khokhar, M. Banakar, W. Cao, J. S. Penades, D. T. Tran, F. Y. Gardes, D. J. Thomson, G. T. Reed, H. Wang, and G. Z. Mashanovich, "Silicon-on-insulator free-carrier injection modulators for the mid-infrared," *Opt. Lett.*, vol. 44, no. 4, p. 915, 2019.
[58] J. Guo and S. G. Tantawi, "Development of ultra-fast silicon switches for active X-band high power RF compression systems," in *Proc. Part. Accel. Conf.*, May 2005, pp. 701–703.
[59] H. Hora, "Refractive index and absorption," in *Laser Plasmas and Nuclear Energy*, Y. Ksander, Ed., Boston, MA, USA: Springer, 1975, pp. 39–51.
[60] C. A. Balanis, *Antenna Theory Analysis and Design*. New York, NY, USA: Wiley, 1997, pp. 258–259.

ZHICHENG SHEN received the M.Eng. degree in electronic engineering from the University of Southampton, U.K., in 2020, where he is currently pursuing the Ph.D. degree in electronic and electrical engineering. He has full access to and experience with Southampton Nanofabrication Centre. His research interests include mm-wave intra-chip and inter-chip interconnect, metamaterial and metasurface, on-chip devices, and micro-fabrication.

SAJJAD TARAVATI (Senior Member, IEEE) received the Ph.D. degree in electrical engineering from Polytechnique Montreal, Montreal, QC, Canada, in 2017. From 2017 to 2018, he was a Postdoctoral Research Fellow with Concordia University, Montreal, where he conducted research on nonreciprocal magnetless electromagnetic systems, space-time modulation, and wave processing techniques. From 2018 to 2019, he was a Postdoctoral Fellow with the University of Toronto, Toronto, ON, Canada, working on multifunctional spatiotemporal metasurfaces and electromagnetic wave manipulation. In 2019, he joined the superconducting quantum computing group with the University of Oxford, U.K., where he was a Postdoctoral Researcher focusing on spatiotemporal superconductors and their applications in quantum computers. He is currently a Lecturer (Assistant Professor) within the Faculty of Engineering and Physical Sciences, University of Southampton, Southampton, U.K. He is the Technological Founder of LATYS Intelligence, a company specializing in versatile and programmable space-time metasurfaces, based on two pioneering patents authored by his. His research interests include space-time metamaterials, metasurfaces, quantum metamaterials, nonreciprocal electromagnetics, and their applications in wireless communications, quantum computing, and sensing. His work has made significant contributions to the field of electromagnetics, particularly in the design and experimental demonstration of nonreciprocal systems and programmable metasurfaces. His innovations have influenced the design of advanced antennas, microwave components, and wireless systems, paving the way for breakthroughs in wireless communications, quantum technologies, and wave-based processing systems. He has published more than 30 first-author journal articles and holds three patents on dynamic metasurfaces. He was a recipient of several prestigious awards, including the Khwarizmi International Award, in 2010, the Outstanding Researcher Student Award from IUST, in 2012, and the Horizon Postdoctoral Fellowship from Concordia University, in 2018. He was recognized for his professional expertise and contributions to the field of electrical engineering. He has been an active contributor to the IEEE community, serving as a speaker and workshop organizer at international conferences, including the 2021 IEEE International Microwave Symposium in Atlanta, GA, USA. He has also been an Instructor with the University of Toronto, the European School of Antennas, and several other institutions, where he has taught a wide range of courses in electromagnetics, telecommunication engineering, and antennas. He leads a research group focused on developing novel space-time metamaterials and metasurfaces for applications in wireless communications and quantum technologies. He also serves as a reviewer for several leading journals in his field.

JIZE YAN received the B.Eng. degree from Tsinghua University and the Ph.D. degree from the University of Cambridge. He is currently a Professor of sensor technology and microsystems with the School of Electronics and Computer Science, University of Southampton. His pioneering research has set several world records, driving innovations in meta-lense and vortex-beam sensors, distributed fiber optic sensors, MEMS/silicon photonic/optomechanical sensors, wireless sensor networks, energy harvesting for sensors, and cleanroom fabrication. As a PI and co-I, he has been awarded more than 28M in research grants, published more than 100 peer-reviewed publications, and earned multiple best-paper awards. He leads a dedicated research team of more than ten Ph.D. Students and Postdoctoral, collaborate with industry leaders to address vital metrology challenges in health care, space observatories, energy safety, and quantum technology. With a portfolio of more than ten patents, he co-founded a few spin-out companies and facilitated technology transfer to industry, resulting in more than 16M income streams. He also serves as an associate editor for five international journals and a member of the EPSRC Review College.